Impact of Offshore Winds on a Buoyant River Plume System

JOSEPH T. JURISA* AND ROBERT J. CHANT

Rutgers, The State University of New Jersey, New Brunswick, New Jersey

(Manuscript received 28 June 2012, in final form 3 May 2013)

ABSTRACT

Idealized numerical simulations utilizing the Regional Ocean Modeling System (ROMS) are carried out to examine the response of buoyant river plume systems to offshore-directed wind stresses. It is found that after a few inertial periods of wind forcing the plume becomes detached from the coast and reaches a steady state in terms of the plume's offshore position, width, and plume-averaged depth, salinity, and velocity. The steady-state offshore position of the plume is a balance between the cross-shore advection driven by the estuarine outflow and the alongshore advection driven by the Ekman velocities, and is described using the ratio of the outflow Froude number and the plume Froude number. The steady-state salinity structure is maintained by a balance between the cross-shore advection of salt creating stratification, the turbulent vertical mixing, and the downstream transport of freshwater continually resetting the system. Plume mixing is also analyzed using a salinity coordinate system to track the changes in freshwater volume in salinity space and time. A dynamical plume region classification is developed with use of a Richardson number–based critical mixing salinity criterion in salinity space. This salinity class–based classification agrees well with a classification based on an alongshore analysis of the salt flux equation. For this classification the near field is dominated by large cross-shore fluxes and the midfield by a diminishing cross-shore salt flux, and in the far field there is a balance between the alongshore salt flux and turbulent mixing.

1. Introduction

When buoyant estuarine water is discharged into the coastal ocean it is deflected to the right (in the Northern Hemisphere) and forms a coastally attached plume that propagates downstream in the direction of Kelvin wave propagation. How this buoyant coastal plume is transported across the continental shelf and eventually mixes with the saltier ambient shelf water is important for the understanding of shelf-wide circulation and biogeochemical processes. Strong vertical velocity shear driven by the estuarine outflow dominates mixing at the mouth of the estuary (MacDonald et al. 2007) and wind is the dominant mixing mechanism in the far-field plume due to the plume's tendency to be confined to a thin surface layer (Garvine 1995; Hetland 2005).

Cross-shelf transport on the shelf is thought to be driven mainly by alongshore winds through an Ekman transport in the surface layer. At the coast, this can lead to an upwelling of bottom water from the bottom layer or a downwelling of water from the surface layer. Downwelling winds impact a buoyant coastal current by transporting the buoyant water against the coast and steepening the isopycnals, leading to an enhanced downstream transport (Moffat and Lentz 2012). Upwelling winds lead to the offshore edge of the plume to mix to a critical depth and begin to be transported offshore. The plume then becomes detached from the coast and the plume continues to entrain salty ambient water and deepen due to mixing on the offshore edge driving by an Ekman straining mechanism. The plume is continually transported across the shelf and mixes until it becomes indistinguishable from the ambient shelf water (Fong et al. 1997; Fong and Geyer 2001; Lentz 2004). Recently, progress has been made in recognizing the effects of cross-shelf winds on driving cross-shelf transport for an unstratified shelf (Tilburg 2003; Fewings et al. 2008). It has been found in nearshore regions where the surface and bottom Ekman layers interact that cross-shore winds can drive a significant cross-shore transport.

* Current affiliation: College of Earth, Ocean, and Atmospheric Sciences, Oregon State University, Corvallis, Oregon.

Corresponding author address: Joseph T. Jurisa, College of Earth, Ocean, and Atmospheric Sciences, Oregon State University, 104 CEOAS Administration Building, Corvallis, OR 97331-5503.
E-mail: jurisa@coas.oregonstate.edu

DOI: 10.1175/JPO-D-12-0118.1

For a surface-advected buoyant river plume, it is not expected that the surface and bottom boundary layers will directly interact, due to the strong stratification in the plume. Because of this, it has been assumed that the cross-shelf transport due to offshore winds is insignificant when compared to alongshore winds because the Ekman transport is directed in the alongshore direction. However, it is still not entirely known how an offshore wind will impact the mixing and freshwater transport of a buoyant river plume. In the pioneering modeling study by Chao (1988) it is noted that an offshore wind leads to a spreading of the plume, but model limitations prevented a more thorough analysis. For a model of the Hudson River plume in the New York Bight with idealized wind and river forcings, it was also found that an offshore wind leads to a spreading of the plume in the cross-shore direction and the downstream velocity maximum in the plume develops near the offshore edge, impacting the freshwater transport (Choi and Wilkin 2007). Cross-shore winds are a common feature globally, manifested as a sea–land breeze system or simply seasonal wind patterns, but the impact of these cross-shore winds on buoyant coastal flows has been a relatively unexplored but important area. In the New York Bight, the dominant wind direction during the winter is toward the east-southeast. When modeling the freshwater transport pathways in the New York Bight, Zhang et al. (2009) found upstream transports along the New Jersey coast during periods of downwelling winds. The model results were only analyzed in the context of alongshore winds, so the upstream transport near the coast contradicts the idea that transport is downstream during downwelling wind events. The fact that the winds in the winter have a significant offshore component suggests that the winter season cannot simply be described as a downwelling season; the offshore component of the wind could play an important role in determining the plume response.

This leaves several questions on the response of a plume system to offshore winds that we plan to answer in this study. How does the plume response evolve in time? What is the role of the estuarine outflow conditions on the far-field plume structure and position? Are the scalings for turbulent mixing, plume depth, and velocity for alongshore winds relevant for cross-shore winds?

Using idealized numerical model domains and forcings, this study will describe the response and structure of a buoyant plume to steady offshore winds. Section 2 will describe the background theory for calculating several plume parameters, section 3 will describe the numerical model and forcing setup, section 4 will examine the model results and compare them to the background theory, and section 5 will discuss the results and their implications.

2. Plume properties

Here we develop scalings for the vertical mixing, plume depth, velocity, and density. These scalings are based on those from studies of the upwelling response of river plumes (Fong and Geyer 2001; Lentz 2004); however, as described in the following sections, these scalings also reasonably describe the response to offshore winds as well. The parameterizations of plume properties in this section are based on results from this study that show that the plume has become detached from the coast in response to the offshore wind stress and has reached a relative steady state in terms of cross-shore plume structure and offshore position after a few inertial periods. Immediately after the onset of the offshore wind stress the plume mixes over the entire base of the plume, while after the plume reaches a steady structure the mixing is confined to the offshore side of the plume where the strong downstream velocities are located (Fig. 1).

a. Plume depth

The depth to which the plume mixes can be calculated using a critical bulk Richardson number parameterization (Pollard et al. 1973; Trowbridge 1992; Fong and Geyer 2001; Lentz 2004):

$$\mathrm{Ri}_c = \frac{g\Delta\rho_0 h_p}{4\rho_a|\Delta u|^2}, \tag{1}$$

where ρ_a is the ambient density, $\Delta\rho_0$ is the density anomaly in the plume immediately after the onset of wind forcing, h_p is the plume thickness on the offshore side of the plume, and Δu is the velocity difference over the thickness of the plume. Here the velocity shear that contributes to the mixing of the plume is considered to be due to wind-driven Ekman velocity, as the geostrophic velocities are assumed to be balanced in a Richardson number sense. Hence, Δu is considered to be $U_e = \tau_w/\rho_a f$ divided by h_c. This alongshore Ekman velocity is substituted into (1) and solved for h_c, yielding an expression for plume thickness:

$$h_p = \left(\frac{4\mathrm{Ri}_c\rho_a U_e}{g\Delta\rho_a}\right)^{1/3}. \tag{2}$$

Here, Ri_c is treated as a constant. The value of Ri_c in plume studies ranges between 0.5 and 3.0 (Fong and Geyer 2001; Lentz 2004; Hetland 2005) and in this study a value of 1.0 is used. The same formulation derived by Fong and Geyer (2001) and Lentz (2004) is used in (2) except here it is shown to be effective for cross-shore wind response that reaches a steady-state structure. As in Fong and Geyer (2001) and Lentz (2004), the plume

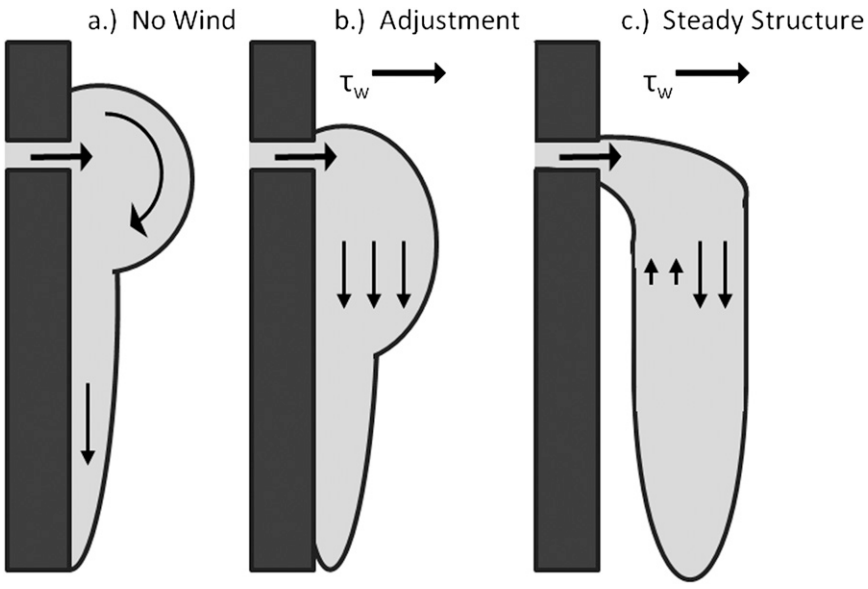

FIG. 1. Schematic of the plume response to an offshore wind stress: (a) no wind, (b) adjustment, and (c) steady structure.

depth is dependent on the balance between the wind-induced velocity shear driving the turbulent mixing and the plume's buoyancy suppressing the turbulent mixing. If the actual plume depth is shallower than the critical Richardson number–based depth calculated in (2), then the plume will mix and deepen until the plume depth matches the critical depth.

b. Plume-averaged velocity

The alongshore velocities in the plume are driven by the cross-shore pressure gradient and the downstream Ekman velocities. While the cross section–averaged cross-shore baroclinic pressure gradient vanishes, the response of the sea surface to the cross-shelf winds results in a nonzero cross shore–averaged barotropic pressure gradient. This allows the plume-averaged velocities to be written as simply the sum of the downstream Ekman velocity and the upstream barotropic velocity due to wind-driven sea level set down at the coast:

$$v_p = v_{\text{Ekman}} + v_{\text{barotropic}}, \tag{3}$$

where

$$v_{\text{Ekman}} = \frac{\tau^{s_x}}{\rho f h_p}. \tag{4}$$

The barotropic velocity can be calculated by

$$v_{\text{barotropic}} = -\frac{g}{f}\frac{\partial n}{\partial x}, \tag{5}$$

where

$$\eta = \frac{u_*^2}{gH}x \tag{6}$$

is from Csanady (1982). Here, τ^{s_x} is the cross-shore wind stress, ρ is the density, f is the Coriolis parameter, g is the gravitational acceleration, η is the sea surface elevation, H is the water depth, and x is the cross-shore distance. The frictional velocity u_* is written as $(\tau^{s_x}/\rho)^{1/2}$.

c. Plume density

The estimate for plume-average density is based on the formulation from Lentz (2004) for a plume response to upwelling winds. This theory is based on a conservation freshwater in a cross-shore transect of the plume,

$$\Delta\rho_o A_o = \Delta\rho_i A_i, \tag{7}$$

where subscript i refers to the initial conditions and subscript o refers to conditions after the onset of wind. This assumption works well for the upwelling wind case because the transect is essentially disconnected from the freshwater source; there is no upstream control in the upwelling case. This is not true for the offshore wind case because the wind is driving a significant downstream freshwater flux that can potentially change dramatically during the first few inertial periods after the onset of the wind stress depending on the initial structure of the plume. This theory of freshwater conservation over time will not work for plumes where the river

discharge is significantly larger than the initial freshwater transport downstream in the plume (there is a large bulge region near the outflow). This setup leads to a large increase in freshwater transport at a downstream transect due to the advection of the bulge region downstream, which this theory does not account for. However, if initially there is no bulge region and the river discharge is close to the freshwater transport in the plume, the assumption of freshwater conservation is a valid one.

Using the theory of freshwater conservation, Lentz (2004) derives an expression for the plume-averaged density difference immediately after the onset of the upwelling wind stress:

$$\Delta\rho_o = \begin{cases} \Delta\rho_i(1+\tilde{h}_p^2)^{-1} & \tilde{h}_p \le 1 \\ \Delta\rho_i(A_i\tilde{h}_p) & \tilde{h}_p > 1 \end{cases}, \tag{8}$$

where $\tilde{h}_p$ is a normalized plume thickness, h_p/h_i at the offshore edge. Because $\Delta\rho_o$ is required to solve for h_p, (8) is substituted into (2), yielding

$$\begin{cases} \tilde{h}_p^3 - \tilde{h}_s^2(\tilde{h}_p^2+1)/2 \approx 0 & \tilde{h}_s \le 1 \\ \tilde{h}_p \approx \tilde{h}_s & \tilde{h}_s > 1 \end{cases}, \tag{9}$$

where $\tilde{h}_s$ is a normalized plume thickness, h_s/h_i, and

$$h_s = \left(\frac{2\mathrm{Ri}_c\rho_a U_E^2}{g h_i \Delta\rho_i}\right)^{1/2}. \tag{10}$$

This reveals a formulation for the plume-averaged density that is only dependent on the initial plume thickness (h_i), density anomaly ($\Delta\rho_i$), and the wind stress (contained in U_E), all the while assuming that the freshwater transport into the cross-shore transect is equal to the freshwater transport out. Please refer to Lentz (2004) for a more thorough derivation and explanation.

3. Model description

In this study, we use the Regional Ocean Modeling System (ROMS; www.myroms.org; Haidvogel et al. 2000; Shchepetkin and McWilliams 2005) to examine the effects of offshore winds on a buoyant plume system. ROMS has been successfully deployed in the past for analyzing both realistic and idealized buoyant river plume (e.g., Choi and Wilkin 2007; Zhang et al. 2009; Hetland 2005).

The model setup used for the idealized simulations uses a 250 km × 225 km domain. The domain includes a 120-km-long channel with a depth of 10 m that serves as the river/estuary. The width of the estuary at the coast varies between 1 and 10 km. The coastline is a straight wall 10 m deep. The domain has a linearly sloping bottom over the shelf region where the depth increases at a rate of 1 m (1000 m)$^{-1}$ (Fig. 2). On the offshore boundary, a radiation boundary condition is implemented for 3D momentum and tracers and Flather (1976) and Chapman (1985) boundary conditions for the free surface and 2D momentum. The boundary is periodic on the up- and downstream boundaries. Over the time frame of the simulations, the buoyant plume does not interact with the boundaries. The model setup utilizes the generic length scale (GLS) *k kl* mixing scheme, which is equivalent to Mellor–Yamada. An M_2 tide is forced on the offshore boundary to simulate more realistic mixing processes. No other shelf circulation is imposed initially at the boundaries. The temperature is set to a constant 10°C throughout the entire domain and the ambient shelf salinity is set to 32.

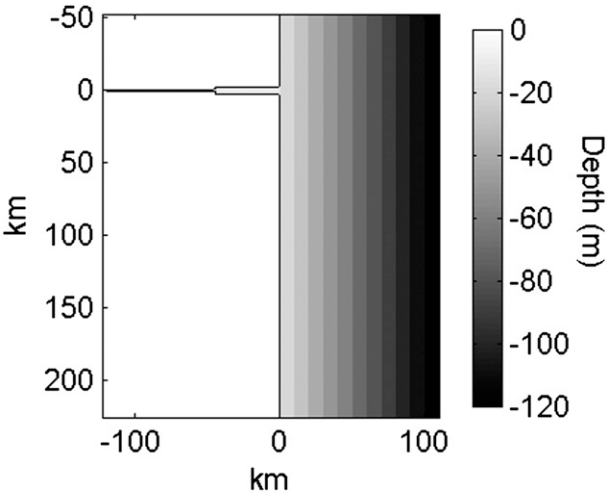

FIG. 2. Model domain bathymetry for idealized ROMS simulations with a 5-km-wide outflow.

The river discharge is forced at the head of the channel with a salinity value of 0 and is held constant over the duration of the run. The model is initialized by running the model with river discharge and no wind forcing until the estuary reaches a steady-state salinity structure. Once the steady-state salinity structure is reached, the shelf salinity is reset to 32 and the shelf velocity and sea surface are set to zero. The model is then run for 2 days to allow a plume to develop on the shelf. The wind forcing is confined to the cross-shore directions. The wind stress is held to zero for the first 4 days of the simulation, allowing for an unforced plume to develop for 6 days. The wind stress is then ramped up over a period of a day to the maximum value where it is held constant for the remainder of the simulation. The

TABLE 1. Summary of model runs with varying river discharge, wind stress, estuary width, and the resultant wind strength index W_{SI}. Runs in boldface signify a W_{SI} value greater than 1.

Model run	Discharge ($m^3 s^{-1}$)	Wind stress ($N m^{-2}$)	Estuary width (km)	W_{SI}
1	500	0.025	1	0.86
2	500	0.05	1	0.93
3	**500**	**0.075**	**1**	**1.11**
4	**500**	**0.1**	**1**	**1.14**
5	**500**	**0.125**	**1**	**1.22**
6	**500**	**0.15**	**1**	**1.3**
7	1000	0.05	1	0.89
8	**1000**	**0.1**	**1**	**1.08**
9	**1000**	**0.15**	**1**	**1.2**
10	1500	0.05	1	0.85
11	**1500**	**0.1**	**1**	**1.08**
12	**1500**	**0.15**	**1**	**1.15**
13	**300**	**0.075**	**5**	**1.03**
14	**300**	**0.125**	**5**	**1.52**
15	500	0.05	5	0.78
16	**500**	**0.1**	**5**	**1.11**
17	**500**	**0.15**	**5**	**1.15**
18	1000	0.05	5	0.85
19	**1000**	**0.1**	**5**	**1.07**
20	**1000**	**0.15**	**5**	**1.28**

ranges of discharge and wind stress values for the offshore wind simulations already completed are listed in Table 1.

4. Results

a. General plume response

Before the onset of the offshore wind stress there is a large, well-defined bulge region near the mouth of the estuary and a narrow coastal current propagating downstream for the narrow outflow simulations. For the wide outflow simulations, the bulge region is more confined and the coastal current is wider, transporting a larger fraction of the freshwater discharge (Figs. 3a and 4a). These initial plume structures generally agree with previous studies on the dependence of plume structure on outflow conditions (Fong and Geyer, 2002; Horner-Devine et al. 2006).

At the onset of the offshore wind stress, the bulge region mixes and is advected downstream and the coastal current is initially slowly advected offshore (Figs. 3b and 4b). After a few inertial periods of wind forcing, the plume structure has now reached a quasi-steady state with respect to the offshore distance, depth, velocity, and salinity. At this point, there is no longer a discernible bulge region near the mouth of the outflow. There is now a strong downstream jet on the offshore side of the plume with a weak (sometimes upstream) flow on the inshore side.

At the onset of wind forcing the plume remains relatively thin, with the wide outflow plumes slightly thicker than the narrow outflow plumes. This difference in thickness is due to the wide outflow cases being more laterally sheared at the outflow than the strongly vertically sheared narrow outflow runs (not shown). This larger vertical velocity shear for the narrow outflows leads to higher shear-induced mixing in the near-field region of the plume. Over the course of the initial response period, the wind-induced vertical velocity shear leads to mixing at the base of the plume, leading to an increase in plume density and a thickening of the plume as seen in far the narrow outflow run 8 in Figs. 5a and 5d

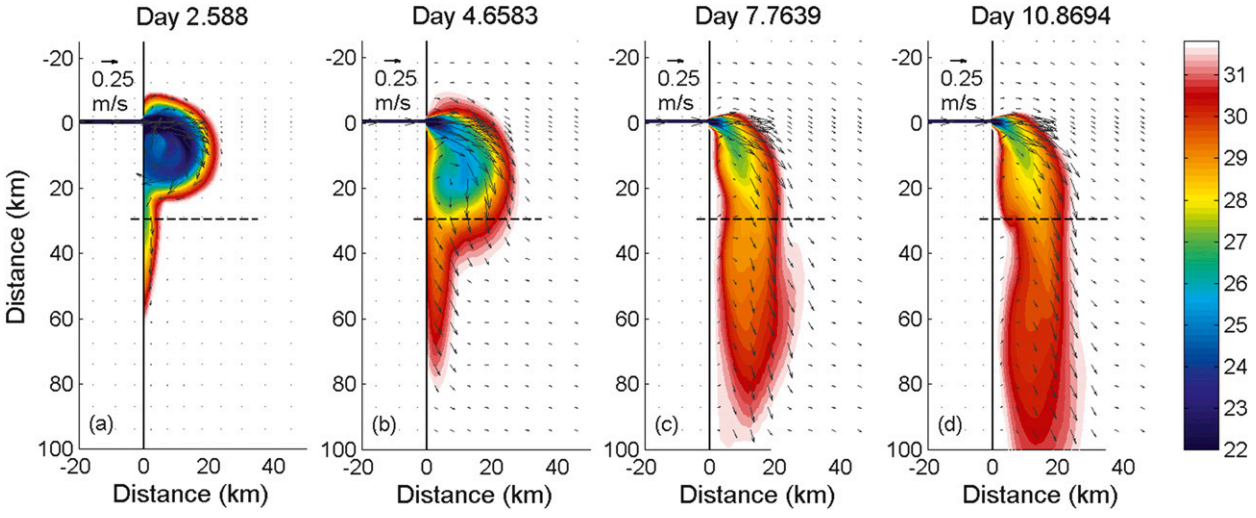

FIG. 3. Tide-averaged surface salinity and velocity for run 8 (1-km-wide estuary, 1000 $m^3 s^{-1}$ discharge, and 0.1 $N m^{-2}$ wind stress) for periods of (a) no wind, (b) onset of wind, (c) 3 days of wind, and (d) 6 days of wind forcing.

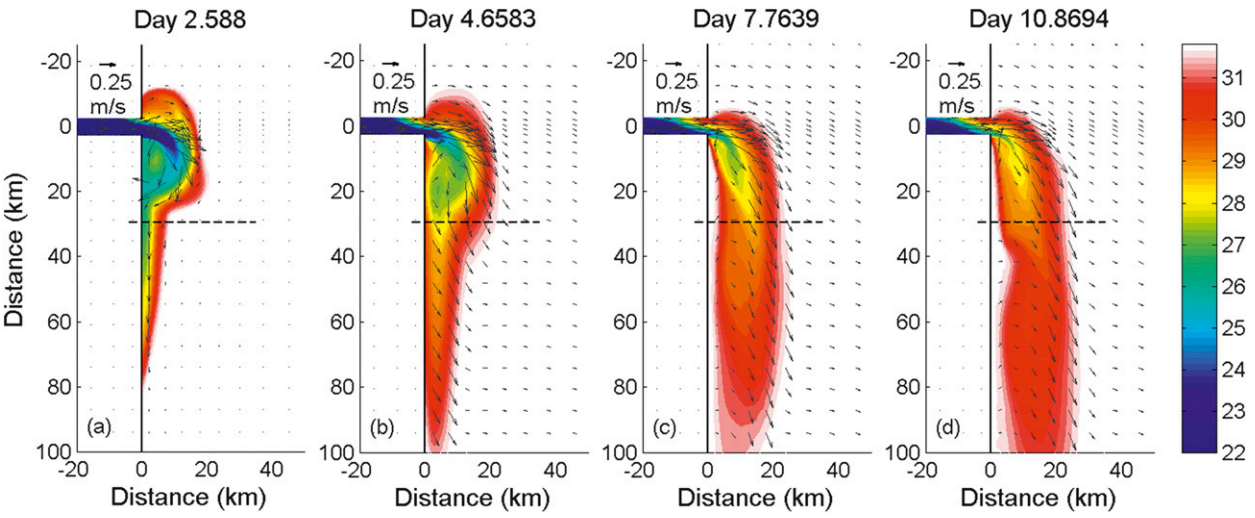

FIG. 4. Tide-averaged surface salinity and velocity for run 20 (5-km-wide estuary, 1000 $m^3 s^{-1}$ discharge, and 0.15 $N m^{-2}$ wind stress) for periods of (a) no wind, (b) onset of wind, (c) 3 days of wind, and (d) 6 days of wind forcing.

when the plume mixes from 4 m deep during the onset of the wind to over 6 m 3 days later. The same is true for the wide outflow case of run 19 that mixes from 5 to 7 m deep (Figs. 6a,d).

During this time period, the plume depth–averaged alongshore velocity structure transitions from a state of weak horizontal shear to one with a strong horizontal shear structure that consists of a strong downstream jet (Figs. 5 and 6). This change in velocity structure over the first few inertial periods is in response to the evolution of the pressure gradients during the time period. Figures 5c, 5f, 6c, and 6f show the cross-shore momentum terms (normalized by f) at the onset of wind forcing and after the spinup period. At the onset of wind forcing, the balance is an Ekman balance between the stress and Coriolis terms. Over a few inertial periods the pressure gradient responds to the wind forcing and the offshore movement of the low salinity core of the plume, yielding a structure that works in concert with the stress term on the offshore side of the plume while working in opposition on inshore side. This interaction between the cross-shore wind-driven stress and pressure gradient terms drive the asymmetric downstream velocity structure observed in the plume. Advective terms, while important in the near field, are negligible in the far field.

b. *Velocity structure*

The cross-shore structure of the alongshore velocity is driven by the cross-shore pressure gradient, wind stress, and Coriolis forcing that drive an asymmetric velocity structure. This is shown through the plume depth–averaged velocities (Figs. 5 and 6), and also from depth-dependent quantities (Fig. 7, middle and bottom panels). The cross-plume velocities are offshore near the surface and onshore at depth, with the circulation being weak on the inshore side of plume and rather vigorous on the offshore side. Plume-averaged quantities are averaged over the plume depth, which is defined as the depth where the cross-shore stress is 10% of the surface value, and the plume width, which is defined as location of the surface 31.8 isohaline.

Vertical profiles of the horizontal velocities are plotted in Figs. 7b–d for three locations in the plume: the midpoint between the inshore edge and the salinity minimum, the salinity minimum, and the midpoint between the salinity minimum and the offshore edge of the plume, respectively. The observed velocity structure can best be described as an Ekman layer for a free surface that is altered by depth-dependent pressure gradients (Ekman 1905). The theoretical depth-dependent Ekman velocities are plotted alongside the observed velocities at the salinity minimum in Fig. 7c. Here we assumed a constant eddy viscosity of 1.3×10^{-3}, which is an average eddy viscosity within the plume from the numerical model, and no pressure gradient for the theoretical velocities. The depth-dependent Ekman velocities capture the general structure of the horizontal velocities. Discrepancies can be due to depth-dependent stratification, eddy viscosity, and pressure gradients, all of which the Ekman formulation does not account for. On the inshore side, the opposing pressure gradient and wind stress lead to weak velocities in both the along- and cross-shore direction. In contrast, on the offshore side both wind stress and baroclinicity work in concert to generate strong currents and vertical shears. The strong wind-driven velocity shear in the alongshore direction

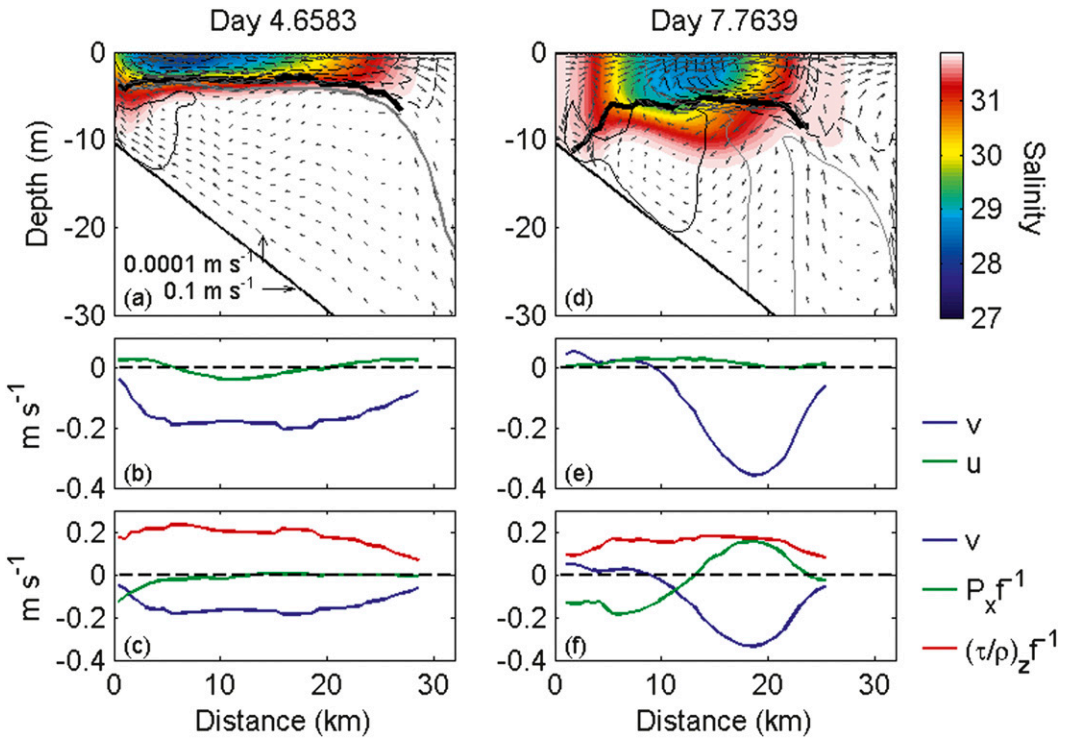

FIG. 5. Plume velocity, salinity, and momentum for run 8 at a cross-shore transect 35 km downstream of the outflow, for (a)–(c) the onset of the offshore wind stress and (d)–(f) 3 days after the onset of the wind stress. For (a) and (d), color signifies salinity. Alongshore velocity is contoured at 0.05 m s^{-1} intervals with dashed contours representing downstream velocity and solid, thin black contours representing upstream velocity. The zero isotach is contoured with the thick gray line. The thick black line signifies the plume depth based on where the cross-shore stress goes below 10% of the surface value. Averaged velocity [in (b) and (e)] and momentum [in (c) and (f)] are vertically averaged between the surface and the plume depth signified by the black line in (a) and (d). The vertically averaged momentum terms are normalized by the Coriolis parameter ($\sim 1 \times 10^{-4}$ s^{-1}) to yield units of m s^{-1}.

on the offshore side of the plume helps drive the strong cross-plume circulation. The Ekman response on the offshore side rotates the currents from the offshore direction at the surface to the onshore direction at the base of the plume and, consistent with this, the alongshore momentum balance here is mainly between the Coriolis acceleration and the vertical stress divergence.

c. *Wind strength influence*

The general plume response to the offshore winds described above only applies to simulations where the cross-shore wind stress is the dominant forcing mechanism; for weaker wind stresses buoyancy forcing can be dominant. During these weaker wind simulations, the wind is not strong enough to significantly alter the initial bulge recirculation region near the mouth of the outflow and a strong offshore jet seen in wind dominant simulations does not develop. Based on these observations, we define a wind strength index based on the ratio of the downstream Ekman velocity and the observed velocity in the plume after the onset of the wind stress:

$$W_{\mathrm{SI}} = v_e / v_p . \tag{11}$$

Here, v_e is the plume-averaged Ekman velocity and v_p is the observed plume-averaged velocity in the plume. This index is the same as the nondimensional wind stress term used in the Garvine (1995) dynamical plume scaling.

In the case when W_{SI} is less than 1, the downstream velocity is larger than the downstream Ekman velocity. During this regime, the plume is not detached from the coast and the cross-shore structure of the plume is asymmetric, leading the cross section–averaged alongshore baroclinic velocities to contribute to the plume-averaged velocity. When W_{SI} is greater than 1, the wind stress is the dominant forcing mechanism and the plume-averaged buoyancy-driven flow is negligible because of the symmetric cross-shore plume structure. In many of our simulations W_{SI} is greater than unity due to upstream barotropic flows driven by the sea level set down near the coast, decreasing the observed plume-averaged velocities.

The value of W_{SI} is listed for each of the model runs in Table 1. For this set of simulations, W_{SI} is less than 1 for

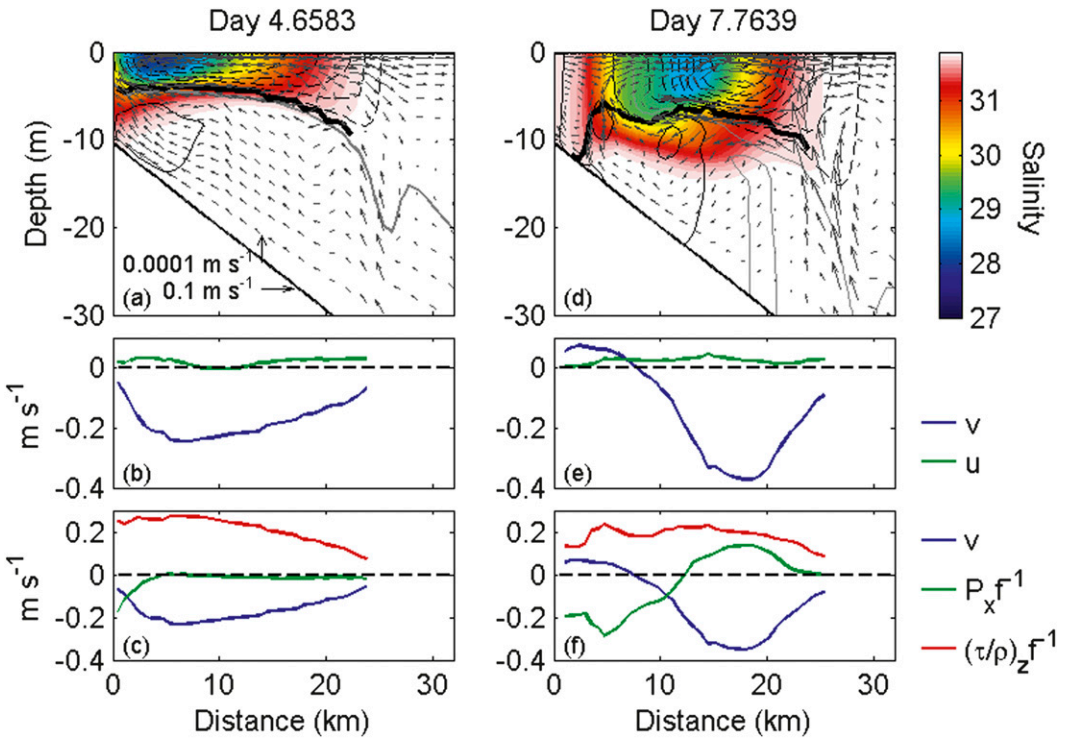

FIG. 6. As in Fig. 5, but for run 20.

wind stresses equal to or less than $0.05\,\mathrm{N\,m^{-2}}$. We choose to not include these runs in the following parameterizations on the plume-averaged velocity, density, width, and offshore position because the theories are based on a wind-dominated plume.

d. Plume-averaged parameters

Plume-averaged depth, velocity, and density are estimated using (2), (3), and (8), respectively, using only the initial plume-averaged depth, density, and wind stress. Here, the critical Richardson number is considered to be 1.0. These theoretical estimates are compared to the plume-averaged parameters from the model at a cross-shore transect located approximately 35 km downstream of the mouth of the estuary at day 7.76, approximately 3 days after the onset of wind forcing (Fig. 8). In general, there is a good agreement between the theoretical depth and the plume depth from the model simulations; however, the theory does tend to slightly overpredict the plume depth, especially for weak wind cases (Fig. 8a).

The theoretical velocity agrees with the model results for strong wind simulations (Fig. 8b). The theory underpredicts the plume-average velocity for weak wind runs and low discharge due to the cross-shore pressure gradient not being symmetrical. In these runs the center of the plume remains close to the coast, which reduces the inshore area of the plume with a shoreward-directed pressure gradients and reduced (or even reversed) alongshore velocity. Consequently this results in a stronger plume-averaged downstream velocity.

As previously stated, the theory greatly overpredicts the density for the narrow outflow runs, while there is a better agreement with the wide outflow runs (Fig. 8c). The best results are for runs 13 and 14, which are both low discharge and wide outflow simulations. These discrepancies are due to the varying validity of the key assumption that freshwater is conserved in the cross-shore transect of the plume. Remember, the simulations are initialized with what amounts to a 6-day-old plume at the onset of the wind stress, and the size of the recirculating bulge region that develops during this time is dependent on the river outflow and the estuary width. Hence, the theoretical density estimates from the large discharge, narrow outflow simulations (runs 10–12) have the greatest offset and the theoretical density estimates for runs 13 and 14 fall the closest to actual plume density values. Despite these errors for the narrow outflows, we can still utilize the estimates of the plume depth, velocity, and density to estimate the plume width for the wide outflow simulations as described in the next section.

e. Plume width

After several days of wind forcing, the freshwater transport in the plume approaches equilibrium with the

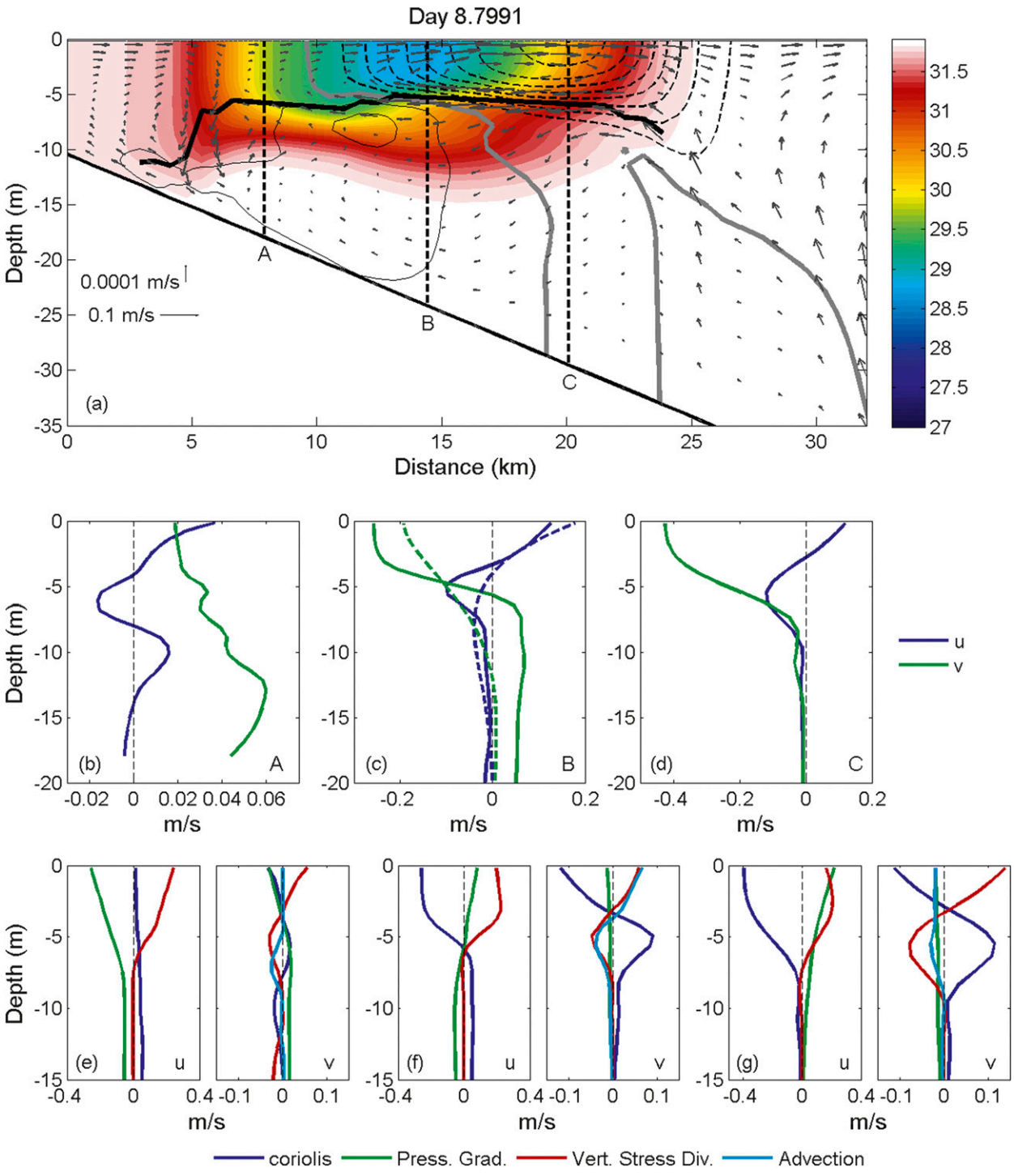

FIG. 7. (a) Plume velocity and salinity for run 8. Color signifies salinity. Alongshore velocity is contoured at 0.05 m s^{-1} intervals with dashed contours representing downstream velocity and solid, thin black contours representing upstream velocity. The zero isotach is contoured with the thick gray line. The thick black line signifies the plume depth based on where the cross-shore stress goes below 10% of the surface value. Vertical dashed lines denote locations of profiles plotted in the other panels. (b)–(d) Profiles of velocity at corresponding locations in (a) and theoretical Ekman velocity profile (dotted). (e)–(g) Cross-shore (u) and alongshore (v) momentum profiles at corresponding locations in (a).

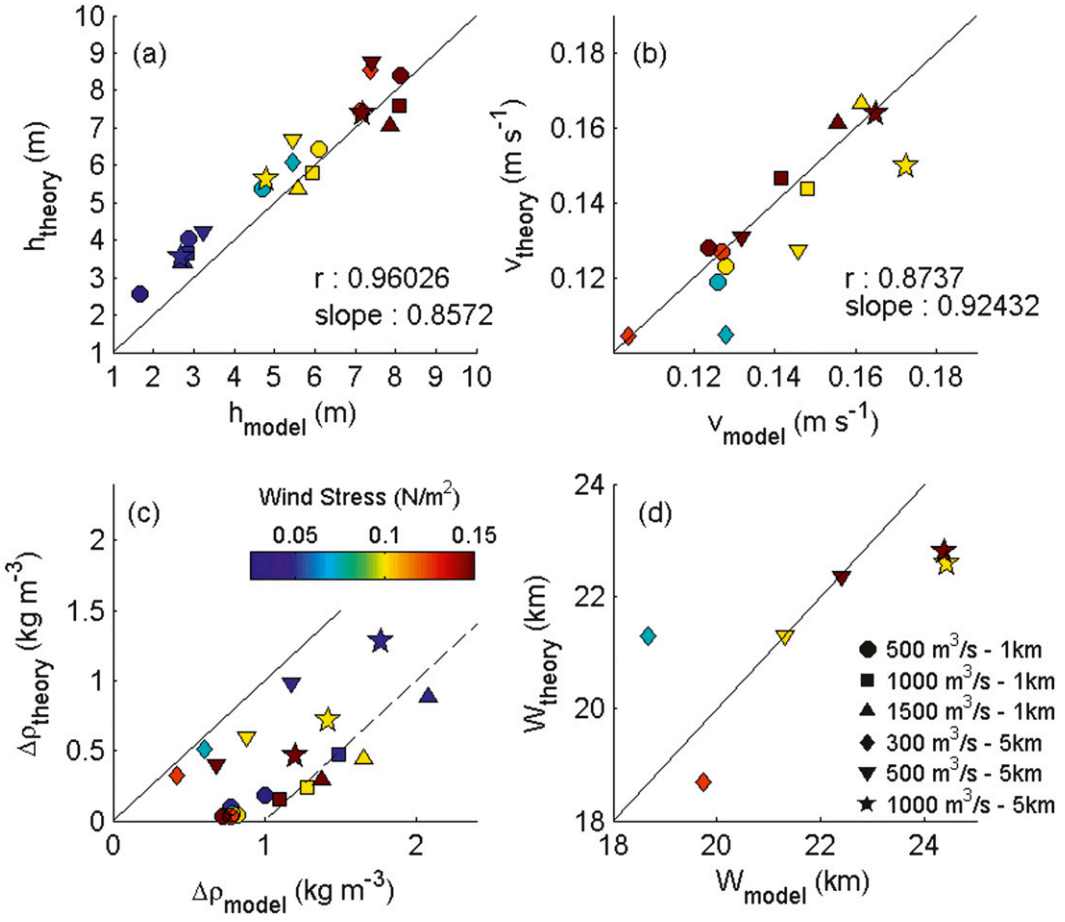

FIG. 8. Comparison of model output and theory for plume (a) depth, (b) velocity, (c) density, and (d) width 4 days after the onset of wind. Shapes indicate the river discharge and estuary width while the color of the marker represents the magnitude of the wind stress. The solid black line is the 1:1 line. The dashed line in (c) denotes a 1 kg m^{-3} offset.

freshwater discharge from the estuary. Knowing this, we can derive a formulation for the freshwater conservation in the plume, assuming that there is no freshwater convergence/divergence in the plume:

$$Q_r = (\Delta s/s_o) v_p h_p W_p . \tag{12}$$

The freshwater discharge from the river is represented by Q_r, and the right-hand side is the freshwater transport through a transect of the plume. The values of v_p, h_p, and Δs are calculated from (2), (3), and (8), respectively. Solving for plume width W_p in (12) yields

$$W_p = \frac{Q_r s_o}{v_p h_p \Delta s}. \tag{13}$$

The results of (13) are computed only for wide outflow runs with $W_{SI} > 1$; these are plotted with the plume width measured in the model in Fig. 8d. Because of instabilities propagating downstream in the plume, the plume widths [as calculated using (13) and from the model] are averaged over a 4-day period. A good agreement with the observed plume widths for runs that are wind dominated is found in (13). The notable exception is run 13 (5-km-wide estuary, 120 m^3 s^{-1} discharge, and 0.1 N m^{-2} wind stress) where the theory greatly overpredicts the plume width. The value of W_{SI} for run 13 is 1.03, so it is near the wind-forced limit, and it can be seen in Fig. 8b that it also has a large offset when comparing the theoretical and model velocities, which leads to an increase in the theoretical plume width.

f. Offshore position

We now have reliable formulations for the plume-averaged depth and velocity for all wind-dominated runs, and salinity and width estimates for low discharge and wide outflow runs. We now will describe the controls of the offshore position of the plume core. The initial offshore transport of the plume can be divided

into two processes: the spinup of the Ekman response and the advection from the estuarine outflow. The steady-state offshore position of the plume core is simply a balance between the offshore advection due to the estuarine outflow and the downstream advection of the plume due to the wind-driven Ekman transport. The offshore advection of the plume due to the estuarine outflow only impacts the plume near the estuarine outflow. Outside of this ''turning region,'' only the downstream advection due to the Ekman transport affects the plume propagation, hence the core of the plume remains parallel to the shore in the far field. The plume's steady structure in response to the offshore winds can be thought of as a baroclinic eddy (the bulge region) that has been elongated by the Ekman transport. Horner-Devine et al. (2006) noted that the offshore position of the bulge core is dependent on the outflow Froude number, so here we parameterize the cross and alongshore advection processes with two Froude numbers:

$$F_{\text{estuary}} = (u/c)_{\text{estuary}} \quad \text{and} \quad F_{\text{plume}} = (v/c)_{\text{plume}}. \qquad (14)$$

Here u is the average outflow velocity at the mouth of the outflow, v is the plume-averaged velocity at a downstream transect, and c is the internal wave speed ($c = \sqrt{g'h}$) at the location denoted by the subscript. The ratio of the two Froude numbers, $F_{\text{plume}}/F_{\text{estuary}}$, can be thought of as a ratio of two nondimensional velocities. With that in mind, the larger the ratio the closer the plume core is to the shore and the smaller the ratio the further offshore the plume core will be.

The ratio is plotted with the normalized offshore distance of the plume core in Fig. 9, where the plume core is defined as the location of the minimum surface salinity at the transect and this position is normalized by the internal deformation radius ($R_{\text{di}} = c/f$). There is a good agreement between the Froude number ratio and the normalized offshore plume core position. If the normalized plume velocity is larger than the normalized estuarine velocity, then the plume will be close to the shore due to the plume being advected downstream faster than it is being advected offshore by the outflow velocity. The opposite is true if the Froude number ratio is less than 1. The variability in the Froude number ration is dominated by F_e for narrow outflow simulations and by F_p for wide outflow simulations.

5. Plume mixing

Understanding mixing is vital to understanding the response of a buoyant plume to a wind stress. To achieve this understanding we follow Hetland (2005) and begin an analysis of the vertical salt fluxes throughout transects of the plume, then classify the vertical salt flux at the base of the plume according to surface salinity, and finally track freshwater transports between salinity classifications.

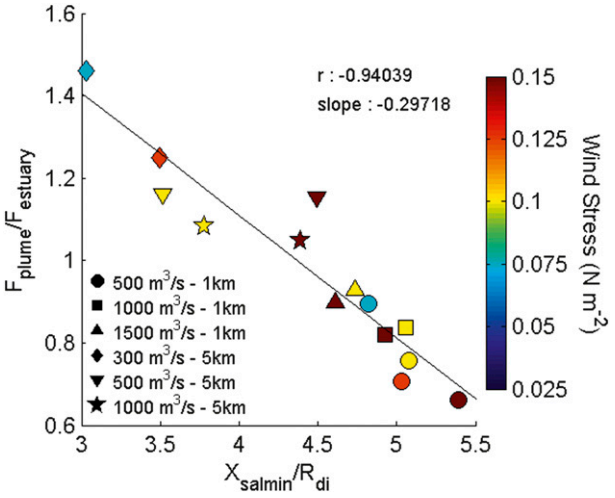

FIG. 9. Ratio of plume and estuary Froude numbers and the normalized offshore position of the plume core. Shapes indicate the river discharge and estuary width while the color of the marker represents the magnitude of the wind stress. The black line is the best-fit line.

a. Cartesian coordinate analysis

The vertical salt flux is calculated by multiplying the hourly salt eddy diffusivity and vertical salinity gradient from the numerical model and then averaging the product over two M_2 tidal cycles. Cross-shore transects of vertical salt fluxes are plotted at two transects in Fig. 10 for three different time periods. Transect 1 is at the mouth of the estuary and transect 2 is approximately 35 km downstream of the outflow.

The highest values of vertical salt flux relative to the rest of the plume are found at transect 1 for run 8 (1-km-wide estuary, 1000 $\text{m}^3\,\text{s}^{-1}$ discharge, and 0.1 $\text{N}\,\text{m}^{-2}$ wind stress) near the outflow region where there is high-velocity shear that drives the mixing. This outflow region encompasses the near-field region of the plume that will be discussed later in this section. The high vertical salt flux values near the outflow region increase after the onset of the wind stress (day 4 and after) due to an increase in the velocity shear. This increase in mixing near the outflow after the onset of the wind stress coincides with an increase in the surface layer salinity. Before the onset of the wind stress at transect 2, the plume is simply in a geostrophic balance that exhibits less vertical mixing in the absence of a surface stress and the vertical velocity shears associated with the estuarine outflow. At day 4.65 (onset of wind), the downstream

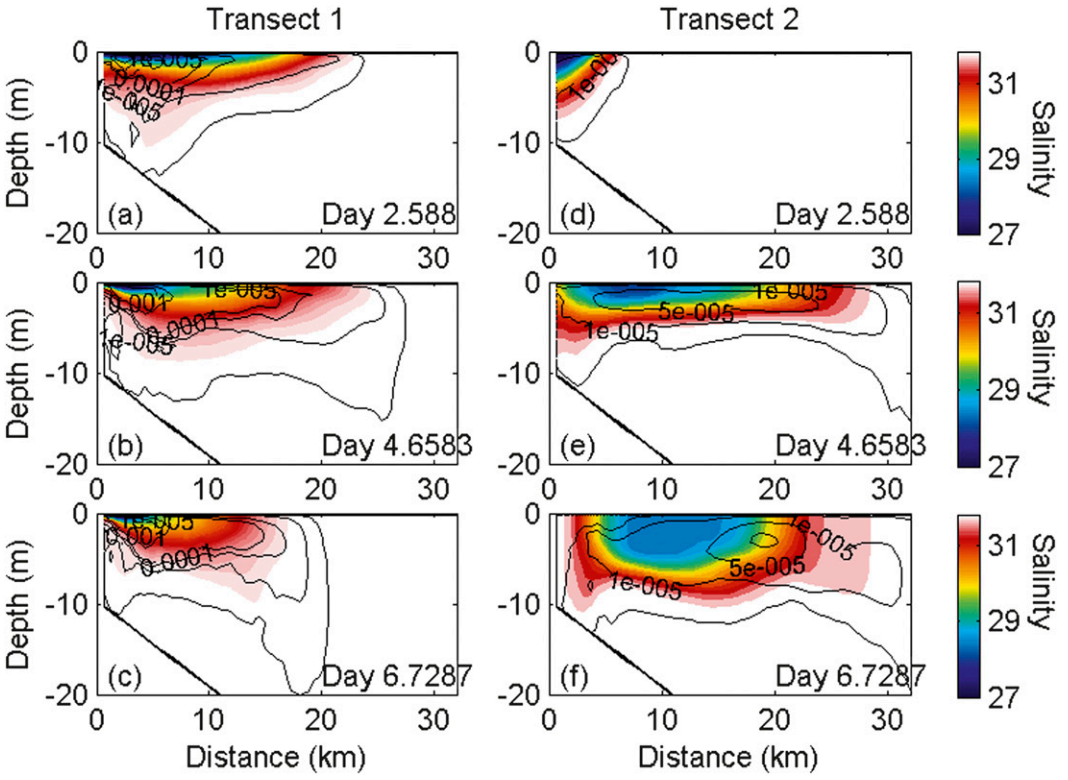

FIG. 10. Vertical salt flux (black contours) and salinity (color map) for run 8 at two cross-shore transects: (a)–(c) near the mouth and (d)–(f) 35 km downstream for three time periods, 2 days before the onset of wind (top), the onset of wind stress (middle), and 2 days after the onset of wind (bottom).

velocity is broadly distributed over the width of the plume from the initial Ekman response and the vertical salt flux mirrors that vertical velocity shear with the highest values distributed widely over the inner portion of the plume transect. After the cross-shore pressure gradients develop and the downstream offshore jet develops, the high mixing rates form on the offshore side of the plume in the vicinity of the high-velocity shear zone described previously.

Even though there are relatively high vertical salt flux values on the offshore side of the plume at a given cross-shore transect, the plume remains remarkably stable in its salinity and velocity structure over time. In examining the salt equation, the importance of the advective terms becomes clear in maintaining the steady salinity field. The first-order balance is between the turbulent vertical mixing $[\partial/\partial z(K_s \partial s/\partial z)]$, the cross-shore advection of salt $(u\partial s/\partial x)$, and the alongshore advection of salt $(v\partial s/\partial y$; Fig. 11). The turbulent mixing is focused on the offshore side of the plume in the high vertical shear region. Here, the vertical mixing that is acting to destratify the plume is roughly balanced by the straining of the salinity field by the cross-shore velocity field that acts to stratify the water column. On the inshore side of the plume there is weak vertical velocity shear and the cross-shore circulation acts to make the plume's isopycnals more vertical, reducing the stratification in the plume and inhibiting vertical mixing of salt in this region of the plume. The residual of $u\partial s/\partial x$ and $\partial/\partial z(K_s \partial s/\partial z)$ is dominated by the alongshore advection of salt $(v\partial s/\partial y)$. While $v\partial s/\partial y$ may appear small, it is vital to maintaining the steady nature of the plume by advecting freshwater from upstream into the transect, allowing $u\partial s/\partial x$ to stratify the offshore portion of the plume, and advecting the saltier mixed water downstream. Once at the steady state, this balance allows the cross-shore salinity structure to constantly maintain itself. This balance is similar to that of a tide-averaged estuarine structure where the downstream advection of freshwater balances the turbulent vertical mixing, allowing the estuary to maintain a steady, stratified salinity structure.

Here, we examine the alongshore structure of the salt equation to describe the different dynamical regions of the plume. We start by using the salt equation of the form

$$\partial s/\partial t = -u\frac{\partial s}{\partial x} - v\frac{\partial s}{\partial y} - w\frac{\partial s}{\partial z} + \partial/\partial z\left(K_s\frac{\partial s}{\partial z}\right), \qquad (15)$$

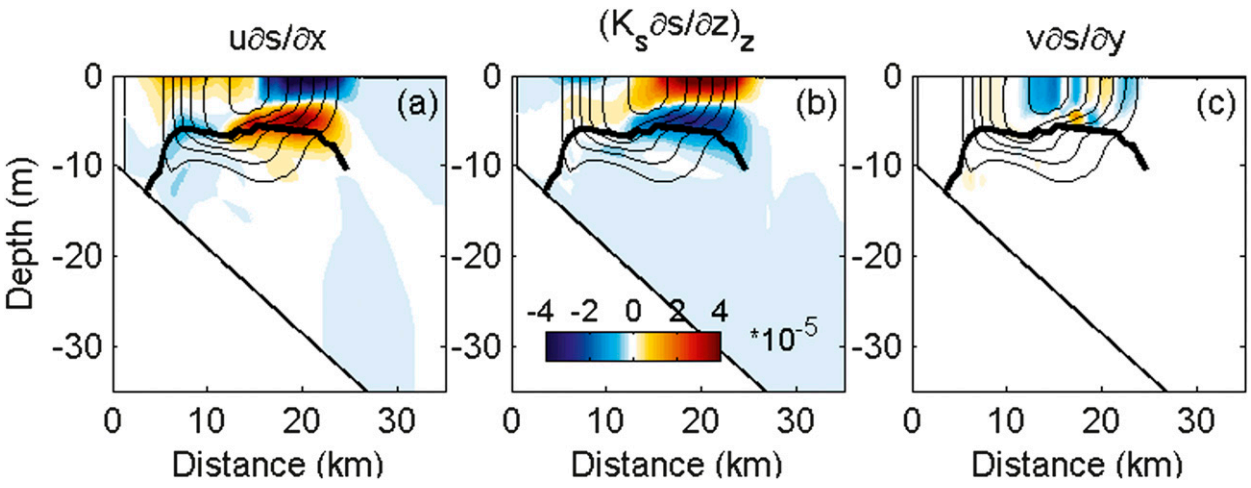

FIG. 11. (a) Cross-shore advective salt term, (b) vertical divergence of the turbulent vertical salt flux, and (c) alongshore advective salt term. Cross-shore transect is located approximately 35 km downstream of the outflow at day 7.76. The thick black line signifies the plume depth based on where the cross-shore stress goes below 10% of the surface value. Salinity is contoured in black at 0.5 intervals.

where x, y, and z are the cross-shore, alongshore, and vertical coordinates, respectively, and K_s is the salinity diffusivity. The terms in (15) are then vertically integrated between the surface and the plume depth as a function of z and then averaged over the depth and width of the plume. This yields the average turbulent vertical salt flux, advective salt fluxes, and the resultant integral of the salt rate within the plume at a given alongshore location. The result of this calculation is shown in Figs. 12d and 12e. Over the alongshore extent of the plume, the main balance is between the vertical turbulent salt flux and the total advective salt flux. In essence, the turbulent mixing is working to destratify the plume while the total advective term is bringing in fresher water from the river discharge to restratify the interior of the plume.

When the advective term is separated into its directional components, different plume mixing regions can be seen. At the location of the outflow, the vertical and alongshore terms are acting to bring salt into the plume, while the cross-shore term is working to freshen the plume. The alongshore term acts to increase the salt content caused by the downstream Ekman flow advecting saltier ambient shelf water from upstream of the outflow into the fresher plume and the plume turning in this region. It should be noted that the lowest plume-averaged salinities do not occur at the outflow, but instead reside 20 km downstream. In the outflow region, there is a net upward vertical velocity in response to the plume thinning and spreading. This can also be described of as the ''lift off'' zone (Hetland and MacDonald 2008; MacDonald et al. 2007). It is this region that we classify as the near field. Here, the cross-shore advection of freshwater from the river outflow dominates the total advective term. The leading-order terms in the near-field region are the total advective term, which is balanced by the turbulent vertical salt flux. The salt rate does not contribute to the balance in this region.

The location where plume spreading and thinning diminishes (vertical advection of salt approaches zero) and the cross-shore advective term approaches zero is the midfield region. Here, the plume is no longer thinning, but the plume is still turning in response to Coriolis- and Ekman-driven flows. The magnitude of the cross-shore salt flux decreases as distance from the near-field region increases because the plume becomes more aligned with the alongshore direction. The alongshore advective term also decreases in the midfield region in response to the alongshore salinity gradient transitioning from a negative (saltier upstream) to a positive (fresher upstream) regime. In the process, the alongshore advective term becomes a dominant term near the downstream limits of the midfield region. The total advective term is once again mainly balanced by the turbulent vertical salt flux; however, the salt rate does play a role and the plume is slightly saltening in this region.

In the far field, the vertical and cross-shore advective salt fluxes are now negligible, and the turbulent vertical salt flux is balanced mainly by the alongshore advective flux of freshwater downstream. In this region of the plume, the alongshore salinity gradient is constant in the alongshore direction. The salinity value near the far-/midfield boundary is constant in time and the salinity value at the leading edge of the plume is 31.8 by the definition we set for defining the plume. These

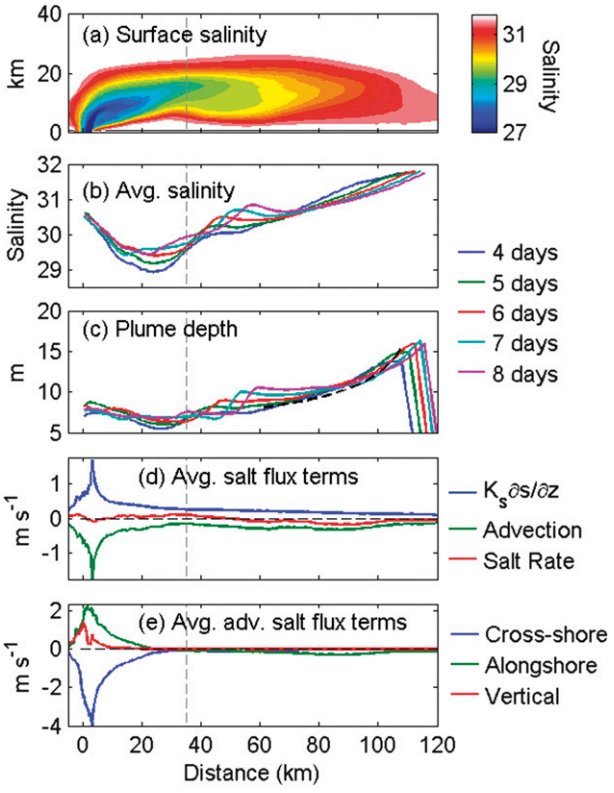

FIG. 12. (a) Surface salinity for run 20 at 4 days after the onset of wind forcing. Cross section–averaged (b) salinity and (c) plume depth for a 5-day time period from 4 to 8 days after the onset of wind. Theoretical plume depth based on a constant salinity gradient is plotted in (c) with a black dashed line. Also shown are cross section–averaged salt flux terms with (d) the total advection term and (e) averaged advective components. Vertical gray dashed line denotes the approximate location of the far-/midfield plume boundary.

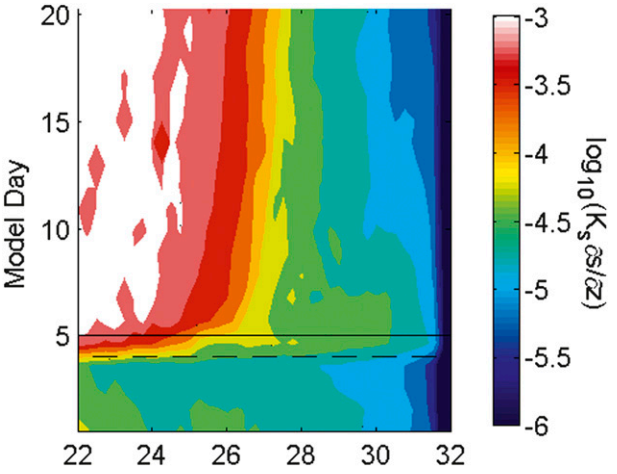

FIG. 13. Vertical salt flux ($m\,s^{-1}$) at the base of the plume classified by salinity for run 8. Horizontal dashed line at day 4 and solid line at day 5 note where the wind stress turns on and reaches its max value, respectively.

factors plus the continually downstream propagation plume (the far field is constantly growing) lead the plume to become fresher in an Eulerian reference frame. It should be noted that the plume structure is dictated by the wind-induced velocity shear mixing processes. If a typical constant salinity gradient in the far-field plume is assumed and used in the critical Richardson number–based estimate of the plume depth, it is found that both the observed plume depth and the theoretical depth show the same $\Delta\rho^{-1/3}$ dependence from (2) (Fig. 12c).

b. *Salinity coordinate analysis*

To look at the both the spatial and temporal variability of mixing in the plume, we examine mean vertical salt fluxes classified by salinity. Using Hetland (2005) as guidance, the vertical salt flux is calculated at the base of the plume over the entire horizontal domain of the plume, excluding the estuary channel. Here, the base of the plume is defined as the depth where $\Delta\rho \leq 1/2(\rho_o - \rho_{\text{surface}})$. The mixing values at the base of the plume are then separated into salinity classes based on the surface salinity at each location ranging from the minimum salinity to the maximum salinity in the model domain, 32, at 0.25 intervals. The results of this analysis are plotted in Fig. 13. Because low salinity values are located near the outflow and higher values are located near the periphery of the plume, we have a general idea of the spatial variability in the mixing at the base of the plume. Generally, the vertical mixing rates in the plume increase when the wind stress is turned on, with the greatest increases seen at the lower salinity classes near the mouth of the outflow. As time progresses, the vertical salt fluxes in the higher salinity classes (far-field plume) decrease to approach the mixing values prior to the wind stress.

To better explain the temporal and salinity space structure of the vertical salt flux, it is helpful to examine the transport of freshwater in the plume in salinity space. The volume of freshwater in an individual salinity class is defined as

$$V_f = \int_{s_{c(i-1)} \leq s < s_{c(i)}} \frac{s_o - s}{s_o} dV, \tag{16}$$

where s_o is the background salinity of 32, s is the salinity of the grid cell, which must fall between salinity class values $s_c(i)$ and $s_c(i-1)$, and V is the volume of the grid cell. Prior to the onset of the wind stress, the freshwater is broadly distributed over a range of salinity classes. After the onset of wind, the freshwater in the lower salinity classes (which represent the recirculating bulge

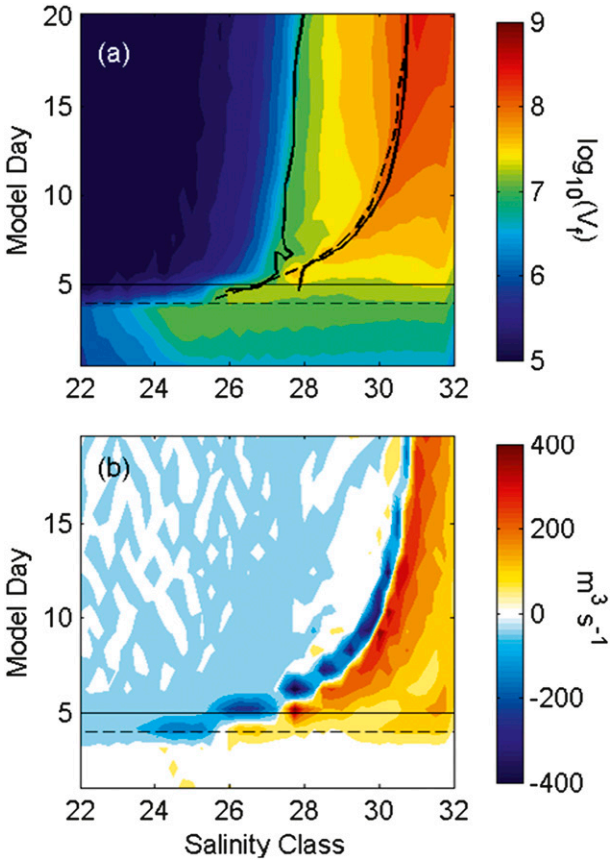

FIG. 14. Freshwater volume (a) dV_f/dt (b) for run 8. Solid and dashed black contours in (a) are the $s_{\text{mix}} = 1.02$ contour and the $dV_f/dt = 0$ contour, respectively. Horizontal dashed line at day 4 and solid line at day 5 note where the wind stress turns on and reaches its max value, respectively.

region) is transported to higher salinity classes (Fig. 14a). This is more obvious when taking the time derivative of V_f. Here, it is clearly seen that there is a loss of freshwater at lower salinity classes and gain at higher salinity classes once the wind turns on (Fig. 14b). It is important to note that there is a clear delineation between salinity classes losing and gaining freshwater. When we take that mixing interface where $dV_f/dt = 0$ and superimpose it on top of the plot of V_f, we can see that it separates regions in salinity space that are steady in time (left of the interface) and still being mixed (right of the interface). In the salinity space, the contours for freshwater volume are vertical in the steady region and horizontal in the unsteady region. This is also true for plume parameters such as plume depth and isohaline surface area (not shown).

The steadiness of the plume parameters can be described by once again manipulating the bulk critical Richardson number formulation in (1). As is done in by Hetland (2005), instead of solving for h_p, (1) can be solved for a critical salinity:

$$s_{\text{crit}} = 32 - \left(\frac{4\text{Ri}_c\rho_a|\Delta u|^2}{gh_p}\right)\beta^{-1}, \tag{17}$$

where $\beta = 0.78\,\text{kg}^{-1}$. The critical salinity is calculated in salinity space by finding the mean depth of the plume at each location in each salinity class based on the mean plume salinity at that location. The salinity space plume depth is then input into (17) along with the Ekman velocity and the critical Richardson number ($\text{Ri}_c = 1$). This yields a critical mixing salinity for each salinity class and time. We develop a critical mixing parameter by taking the ratio of the critical salinity and the salinity class value to yield

$$s_{\text{mix}} = \frac{s_{\text{crit}}}{s_{\text{class}}}. \tag{18}$$

When $s_{\text{mix}} < 1$, the plume will mix because the critical salinity is less than the plume salinity, allowing the wind-induced velocity shear to mix the plume. When $s_{\text{mix}} > 1$, the plume is considered stable because the plume salinity is less than the critical salinity; the velocity shear cannot overcome the buoyancy forcing, preventing the freshwater from being transported to a higher salinity class.

The $s_{\text{mix}} = 1.02$ contour is plotted with the freshwater volume and the $dV_f/dt = 0$ contour in Fig. 14a. The s_{mix} contour closing follows the dV_f/dt contour, which separates vertical contours of V_f (steady in time) and horizontal contours (mixing). This exercise can also be done by calculating a Richardson number in salinity space and contouring a critical value. This approach yields similar results as the critical salinity calculation shown here. In the stable region the wind has mixed the plume enough that the plume salinity is less than the critical salinity, which now inhibits the mixing. The stable regions in salinity space can be loosely defined as the near- and midfield plume regions defined and the mixing region in salinity space can be described as the far-field region. Mainly, the mixing region in salinity lies near the downstream edge on the plume and the periphery. The two classifications cannot be directly compared because salinity classes can reside in different dynamical regions; however, the salinity class classification does provide a general overview of the processes occurring in Cartesian space.

6. Summary

This study has utilized idealized model simulations to describe the response of an offshore wind on a buoyant plume system. The tools developed here to describe and predict the structure of a plume should be applicable to

a plume subjected to an offshore wind stress in nature. The theories should hold for any plume and offshore wind stress that has a wind strength index greater than 1. However, we do acknowledge the difficulties with estimating the plume width because the assumption that the freshwater is conserved in a cross-shore transect is not always the case, due to a supply of freshwater from the estuarine discharge and bulge region.

The idea of the position of the plume core (under a cross-shore wind stress) being related to the outflow velocity of the estuary is in line with the findings of Horner-Devine et al. (2006). For an unforced plume (no wind stress), they found that the offshore position of the core of the recirculating bulge region had a dependence on the outflow Froude and Rossby numbers. Their reasoning was similar in that the offshore position was related to the offshore advection from the outflow and the tendency of the flow to turn right due to rotation. In this study we have added another level of complexity with the addition of the cross-shore wind stress, but the dependence on the outflow velocity remains fundamentally the same.

The dependence of a plume's downstream structure and position on outflow conditions when subjected to an offshore wind stress highlights the importance of the alongshore variability and advection. Historically, the alongshore wind response of the plume has been thought of as strictly two-dimensional (Fong and Geyer 2001; Lentz 2004; Moffat and Lentz 2012). We have shown here that a two-dimensional approach would not capture the entire response of the plume to the offshore wind stress because the alongshore advection of momentum and salt within the plume are first-order parameters in the momentum and salt balances. This result potentially opens up examination of the importance of alongshore variability and advection in the response of a river plume to alongshore wind stresses.

It has been found that the steady salinity structure within a cross-shore transect of the plume is maintained by a balance between the turbulent vertical mixing and the cross-shore advection of salt. The residual is dominated by the alongshore advective term which replenishes the plume transect with freshwater, maintaining the salinity structure in time. By examining the alongshore structure of the cross section–averaged salt flux terms, the plume can be segregated into three distinct regions: near-field, midfield, and far-field plume. The near-field region is located at the outflow of the estuary into the ocean and is characterized by large cross-shore salt fluxes along with high turbulent vertical salt fluxes. The midfield is a transition zone where the plume is turning toward the alongshore direction and thus the cross-shore salt flux diminishes in importance over the region. Once the cross-shore salt fluxes approach zero, the plume reaches the far field. Here, the turbulent vertical salt fluxes are balanced by the alongshore advection of freshwater.

Mixing in the plume was also examined by tracking the volume of freshwater using a salinity coordinate system. A mixing interface in salinity space develops where $dV_f/dt = 0$ and separates regions of the plume that are steady and unsteady in time. The $dV_f/dt = 0$ contour also agrees with a critical mixing salinity that shows whether a salinity class's buoyancy will inhibit mixing (steady) or lead to an increase in plume depth in time (unsteady).

The fact that the plume reaches a relatively steady state can in part be attributed to the dependence on the outflow conditions or an upstream control of the downstream conditions. The steadiness of the plume is also vastly different than the response of a plume to upwelling winds that continuously mix and deepen a plume while transporting it across the shelf. For example, it is shown here that for an offshore wind stress of $0.1\,\mathrm{N\,m^{-2}}$, the plume is rapidly advected offshore 15–20 km but then stays stationary at that location for the duration of the wind event. In contrast, an upwelling wind of the same magnitude and initial plume structure and can be transported offshore approximately 40 km in a 3-day period. This difference can have implications for stratification in the inner-shelf/nearshore region, as well as nutrient transport, productivity, and the fate of pollutants.

Acknowledgments. The authors thank Weifeng Zhang, John Wilkin, and Eli Hunter for help with the model setup, as well as Rob Hetland and an anonymous reviewer for their thoughtful comments on the manuscript. JTJ was supported by NSF Grants OCE-1019179 and OCE 0825833 and by the Institute for Marine and Coastal Sciences. Support for this work was also provided by OCE-0238957.

REFERENCES

Chao, S.-Y., 1988: Wind-driven motion of estuarine plumes. *J. Phys. Oceanogr.,* **18,** 1144–1166.

Chapman, D. C., 1985: Numerical treatment of cross-shelf open boundaries in a barotropic coastal ocean model. *J. Phys. Oceanogr.,* **15,** 1060–1075.

Choi, B. J., and J. L. Wilkin, 2007: The effect of wind on the dispersal of the Hudson River plume. *J. Phys. Oceanogr.,* **24,** 1878–1896.

Csanady, G. T., 1982: *Circulation in the Coastal Ocean.* D. Reidel, 276 pp.

Ekman, V. W., 1905: On the influence of the earth's rotation on ocean currents. *Ark. Mat. Astron. Fys.,* **2,** 1–53.

Fewings, M., S. J. Lentz, and J. Fredericks, 2008: Observations of cross-shelf flow driven by cross-shelf winds on the inner continental shelf. *J. Phys. Oceanogr.,* **38,** 2358–2378.

Flather, R. A., 1976: A tidal model of the northwest European continental shelf. *Mem. Soc. Roy. Sci. Liege,* **6,** 141–164.

Fong, D. A., and W. R. Geyer, 2001: Response of a river plume during an upwelling favorable wind event. *J. Geophys. Res.,* **106,** 1067–1084.

——, and ——, 2002: The alongshore transport of freshwater in a surface-trapped river plume. *J. Phys. Oceanogr.,* **32,** 957–972.

——, ——, and R. P. Signell, 1997: The wind-forced response on a buoyant coastal current: Observations of the western Gulf of Maine plume. *J. Mar. Syst.,* **12,** 69–81.

Garvine, R. W., 1995: A dynamical system for classifying buoyant coastal discharges. *Cont. Shelf Res.,* **15,** 1585–1596.

Haidvogel, D. B., H. G. Arango, K. Hedstrom, A. Beckmann, P. Malanotte-Rizzoli, and A. F. Shchepetkin, 2000: Model evaluation experiments in the North Atlantic Basin: Simulation in nonlinear terrain following coordinates. *Dyn. Atmos. Oceans,* **32,** 239–281.

Hetland, R. D., 2005: Relating river plume structure to vertical mixing. *J. Phys. Oceanogr.,* **35,** 1667–1688.

——, and D. G. MacDonald, 2008: Spreading in the near-field Merrimack River plume. *Ocean Modell.,* **21,** 12–21.

Horner-Devine, A. R., D. A. Fong, S. G. Monismith, and T. Maxworthy, 2006: Laboratory experiments simulating a coastal river inflow. *J. Fluid Mech.,* **555,** 203–232.

Lentz, S. J., 2004: The response of buoyant coastal plumes to upwelling favorable winds. *J. Phys. Oceanogr.,* **43,** 2458–2469.

MacDonald, D. G., L. Goodman, and R. D. Hetland, 2007: Turbulent dissipation in a near-field river plume: A comparison of control volume and microstructure with a numerical model. *J. Geophys. Res.,* **112,** C07026, doi:10.1029/2006JC004075.

Moffat, C., and S. J. Lentz, 2012: On the response of a buoyant plume to downwelling-favorable wind stress. *J. Phys. Oceanogr.,* **42,** 1083–1098.

Pollard, R. T., P. B. Rhines, and R. O. R. Y. Thompson, 1973: The deepening of the wind-mixed layer. *Geophys. Fluid Dyn.,* **3,** 381–404.

Shchepetkin, A. F., and J. C. McWilliams, 2005: The Regional Oceanic Modeling System (ROMS): A split-explicit, free-surface, topography-following coordinate oceanic model. *Ocean Modell.,* **9,** 347–404.

Tilburg, C. E., 2003: Across-shelf transport on a continental shelf: Do across-shelf winds matter? *J. Phys. Oceanogr.,* **33,** 2675–2688.

Trowbridge, J. H., 1992: A simple description of the deepening and structure of a stably stratified flow driven by a surface stress. *J. Geophys. Res.,* **97,** 15 529–15 543.

Zhang, W. G., J. L. Wilkin, and R. J. Chant, 2009: Modeling the pathways and mean dynamics of river plume dispersal in the New York Bight. *J. Phys. Oceanogr.,* **39,** 1167–1183.